Materials Science & Engineering C 117 (2020) 111335

Contents lists available at ScienceDirect

Materials Science & Engineering C

journal homepage: www.elsevier.com/locate/msec

Synthesis, chemical and biochemical characterization of Lu_2O_3-iPSMA nanoparticles activated by neutron irradiation

A. Ancira-Cortez[a,b], G. Ferro-Flores[a,*], N. Jiménez-Mancilla[c,**], E. Morales-Avila[b], D. Trujillo-Benítez[a,b], B. Ocampo-García[a], C. Santos-Cuevas[a], A. Escudero-Castellanos[a], M. Luna-Gutiérrez[a]

[a] Departamento de Materiales Radiactivos, Instituto Nacional de Investigaciones Nucleares, Estado de México 52750, Mexico
[b] Facultad de Química, Universidad Autónoma del Estado de México, Estado de México 50180, Mexico
[c] Cátedras CONACyT, Instituto Nacional de Investigaciones Nucleares, Estado de México 52750, Mexico

ARTICLE INFO

Keywords:
Lu_2O_3 nanoparticles
iPSMA peptide
$^{177}Lu_2O_3$-iPSMA nanoparticles
Radioluminescence
Targeted radiotherapy

ABSTRACT

Among the nanomaterials, rare sesquioxides (lanthanide oxides such as Lu_2O_3) are of interest due to their adequate thermal conductivity, excellent chemical stability, and high light output. The prostate-specific membrane antigen (PSMA) is an integral multifunctional protein overexpressed in various types of cancer cells. The radiolabeled PSMA inhibitor peptides (iPSMA) have demonstrated their usefulness as specific probes in the treatment and detection of a wide variety of neoplasms, mainly due to their high *in vivo* recognition by the PSMA protein.

The objective of this research was to synthesize Lu_2O_3-iPSMA nanoparticles (NPs) and characterize their physicochemical properties before and after neutron activation, as well as to assess their biodistribution profile and *in vitro* potential to target cells overexpressing PSMA. The Lu_2O_3 NPs were synthesized by the precipitation-calcination method and conjugated to the iPSMA peptide using DOTA (1,4,7,10-tetraazocyclodecane-*N*,*N*′,*N*″,*N*‴-tetraacetic acid) as a linking agent. Results of the physicochemical characterization by FT-IR and UV–Vis spectroscopies, SEM, TEM, DLS, HRTEM, SAED, DSC-TGA, and X-ray diffraction indicated the formation of Lu_2O_3-iPSMA NPs (diameter of 29.98 ± 9.07 nm), which were not affected in their physicochemical properties after neutron activation. $^{177}Lu_2O_3$-iPSMA NPs showed high affinity (K_d = 5.7 ± 1.9 nM) for the PSMA protein, evaluated by the saturation assay on HepG2 hepatocellular carcinoma cells (PSMA-positive). The biodistribution profile of the nanosystem in healthy mice showed the main uptake in the liver. After irradiation, radioactive Lu_2O_3-iPSMA NPs exhibited radioluminescent properties, making the *in vivo* acquisition of their biodistribution, *via* optical imaging, possible. The results obtained from this research validate the execution of additional preclinical studies with the objective of evaluating the potential of the $^{177}Lu_2O_3$-iPSMA NPs for the targeted radiotherapy and *in vivo* imaging of tumors overexpressing the PSMA protein.

1. Introduction

Modified and/or functionalized nanomaterials for biological research and biomedicine have been tailor-made for specific purposes, mainly in the treatment of cancers through nanomaterial-based systems for targeted drug delivery and the enhancement of bioimaging [1].

Among the nanomaterials, rare sesquioxides, also called lanthanide oxides (RE_2O_3), are of interest due to their physical and chemical properties, such as excellent chemical stability, adequate thermal conductivity, and high light output [2–4]. Lutetium is the last member of the lanthanide series, being a typical lanthanide since its only common oxidation state is +3, in agreement with its electronic configuration ($[Xe]4f^{14}5d^{1}6s^{2}$) [5]. Due to the physicochemical properties of lutetium, such as density, low thermal expansion, melting point, high phase stability, and a wide gap band, among others, it has been employed to design nanomaterials (core/shell, Lu^{+3}-dopped nanomaterials); these

* Correspondence to: G. Ferro-Flores, Departamento de Materiales Radiactivos, Instituto Nacional de Investigaciones, Nucleares Carretera México-Toluca S/N. La Marquesa, Ocoyoacac, Estado de México C.P. 52750, Mexico.
** Correspondence to: N. Jiménez-Mancilla, Cátedras CONACyT, Instituto Nacional de Investigaciones Nucleares, Carretera México-Toluca S/N. La Marquesa, Ocoyoacac, Estado de México, C.P. 52750, Mexico.
E-mail addresses: guillermina.ferro@inin.gob.mx (G. Ferro-Flores), nallely.jimenez@inin.gob.mx (N. Jiménez-Mancilla).

https://doi.org/10.1016/j.msec.2020.111335
Received 31 May 2020; Received in revised form 30 July 2020; Accepted 1 August 2020
Available online 07 August 2020

engineered nanoparticles have been used in catalysis, optical encoding, biodetection, bioimaging, energetic applications and medical applications [6–9].

The recent advances in nuclear medicine are focused on the design of targeted radiotherapies, for which different biomolecules radiolabeled with beta emitters (^{131}I, ^{90}Y, ^{177}Lu, and ^{188}Re) are employed in the treatment of malignant diseases [10,11]. Lutetium-177 (^{177}Lu) is a radionuclide with suitable nuclear decay characteristics: a half-life ($T_{1/2}$) of 6.71 d, a β_{max} emission of 497.1 KeV (78%), with fewer side effects when compared to external radiation therapy, and a γ radiation of 208 KeV (11%) that can be used for scintigraphy and dosimetry [5,10,11]. ^{177}Lu has been successfully used for radiotherapy, with an effective crossfire effect in cancer cells [11–13].

The prostate-specific membrane antigen (PSMA), also known as glutamate carboxypeptidase II (GCP II), is an integral multifunctional and transmembrane protein [14–16]. It is usually expressed in the epithelial cells of the prostate gland and is overexpressed in 95% of metastatic prostate cancers, correlating its expression levels with androgen dependence and illness progression [14,17,18]. Due to the enzymatic activity of PSMA in its extracellular domain, it can be considered as a molecular target for the binding of antibodies, inhibitors (like iPSMA) and aptamers, which allow the selective delivery of specific therapeutic and diagnostic agents to prostate cancer, as well as to other types of neoplasms, such as gliomas, hepatic carcinomas, osteosarcomas, thyroid cancer, and metastatic breast cancer [14,15,19].

The neutron activation of Lu_2O_3 nanoparticles could be useful to obtain $^{177}Lu_2O_3$ nanoparticles (NPs) and, if the physicochemical characteristics of the lanthanide oxide nanoparticles were not affected by the irradiation procedure, the synthesis of $^{177}Lu_2O_3$-iPSMA NPs could make possible their use for molecular imaging (optical and nuclear) and therapy of cancer cells overexpressing the PSMA protein.

This objective of this research was to synthesize Lu_2O_3-iPSMA NPs and characterize their physicochemical properties before and after neutron activation, as well as to assess their biodistribution profile and *in vitro* potential to target cells overexpressing PSMA.

2. Materials and methods

2.1. Synthesis of Lu_2O_3 nanoparticles

The Lu_2O_3 nanoparticles were synthesized following the precipitation-calcination method, using precursor solutions of $^{nat}LuCl_3$ (Sigma-Aldrich Chemical Co. USA) and NH_4OH:$(NH_4)_2CO_3$. For the first part of the process, the precipitation of the lanthanide was carried out by adding a concentrated 2 M NH_4OH:$(NH_4)_2CO_3$ solution in a molar ratio 1:1, dropwise, to a 5 mM $LuCl_3$ solution under vigorous stirring at room temperature until precipitation (pH = 9) occurred. After the appearance of the sediment, the mixture was stirred for 30 more minutes. Then, the precursor suspension was washed with deionized water three times *via* centrifugation (2500*g*/30 min). Afterward, the sample was heated to 110 °C for 24 h, to be finally heated at 1100 °C for 24 h to complete the calcination process. The sample was stored for later use.

2.2. Neutron activation of Lu_2O_3 nanoparticles/$^{177}Lu_2O_3$ NPs preparation

$^{177}Lu_2O_3$ NPs were produced by neutron capture. The irradiation of $^{nat}Lu_2O_3$ NPs (100 mg) was performed in the SIFCA position of the TRIGA Mark III reactor at ININ (Instituto Nacional de Investigaciones Nucleares, México) at a neutron flux of 1×10^{13} n·s^{-1}.cm^{-2} for 20 h.

2.3. Preparation of $^{177}Lu_2O_3$-iPSMA nanoparticles ($^{177}Lu_2O_3$-iPSMA NPs)

To achieve specificity and enhanced efficacy of the material, $^{177}Lu_2O_3$ NPs were functionalized with the 1,4,7,10-tetraazocyclodecane, *N,N′,N″,N‴*-tetraacetic-acid-hydrazinonicotinyl-Lys(β-naphthylalanine)-NH-CO-NH-Glu (DOTA-HYNIC-iPSMA) peptide sequence [20]. This peptide was designed at ININ (Mexico) and synthesized by Ontores Biotechnology Co. Ltd. (Zhenjiang, China) with a purity of > 98%. Briefly, a suspension of $^{177}Lu_2O_3$ NPs was prepared with a 5 mM sodium citrate solution and homogenized for 30 min using a high-intensity ultrasound probe. Then, the DOTA-HYNIC-iPSMA (iPSMA) peptide was dissolved to obtain a solution at a 1 mg/mL concentration, and 100 μL of the solution was added to the aqueous suspension. The mixture was homogenized using a high-intensity ultrasound probe for 30 more minutes, and after that, the samples were purified by ultrafiltration (centrifugal filter unit MWCO 100 kDa, Merck-Millipore) at 2500 g for 30 min. Finally, samples were stored for later characterization.

2.4. Physicochemical characterization

To obtain evidence of the core's formation and peptide conjugation, as well as to elucidate the physicochemical properties, the following techniques were used to analyze Lu_2O_3 NPs, Lu_2O_3-iPSMA NPs, and $^{177}Lu_2O_3$-iPSMA NPs.

2.4.1. Size, morphology and zeta potential of nanoparticles

Transmission Electron Microscopy (TEM) with a JEOL JEM 2010 HT microscope operating at 200 kV, to observe the two-dimensional relative size and morphology, was used for nanoparticle analysis. Samples of nanoparticles in solution were prepared by evaporating a drop on a carbon-coated TEM copper grid. At least 600 nanoparticles were measured using the ImageJ software, to determine their mean diameter. Moreover, for morphology evaluation, nanoparticles were analyzed by Scanning Electron Microscopy (SEM) with a JEOL JSM 6510LV microscope operating at 20 Kv; the samples were sputtered with a thin layer of gold (~15 nm) using a Denton Vacuum DESK IV system.

The hydrodynamic diameter and zeta potential (ζ) parameters were measured by Dynamic Laser Scattering (DLS) using a “Nanotrac” analyzer (Nanotrac wave, Model MN401; Microtrac; FL, USA). The measurements were performed with aqueous solutions (n = 3), with a wavelength of 657 nm at 21 °C, a current of 15.79 mA, an electric field of 14.38 V/cm, and a sampling time of 128 μs.

2.4.2. Chemical composition

To describe the parameters of the chemical decomposition reactions from $Lu(OH)(CO_3)$ and $Lu_2(CO_3)_3$ to the Lu_2O_3 NPs, the Differential Scanning Calorimetry coupled to Thermogravimetric Analysis (DSC-TGA) technique was used (STD Q600 Instrument), with a heating rate of 10 °C/min in the range of 20 °C to 1000 °C under a nitrogen atmosphere.

For evaluation of the Lu_2O_3 nanoparticle crystal structure, High-Resolution Transmission Electron Microscopy (HRTEM) and Selected Area Electron Diffraction (SAED) patterns were acquired with a JEOL JEM 2010 HT microscope operating at 200 kV.

X-ray diffraction was conducted to determine the crystal parameters of Lu_2O_3 NPs using a CuKα X-Ray source (λ = 0.15406 nm), with an operating voltage kept at 35 kV and a current of 25 mA, respectively, from 2θ = 15 °C to 90 °C in a Bruker D8 DISCOVER diffractometer.

Fourier Transform Infrared (FT-IR) spectra were obtained on a PerkinElmer System 2000 spectrometer (Pike Technologies) with an ATR platform (Attenuated Total Reflection Fourier Transform Infrared) from dried samples. The spectra were obtained from 50 scans at a 1-cm^{-1} resolution and an operating range of 4000–400 cm^{-1}.

Ultraviolet-Visible absorption (UV–Vis) spectra were obtained on a PerkinElmer LambdaBio spectrometer (PerkinElmer; Waltham, Massachusetts, USA) in the range of 200–700 nm (1-cm quartz cuvette).

2.5. Biochemical characterization

2.5.1. Cell culture

The HepG2 cell line of hepatocellular carcinoma (ATCC® HB-

8065™) (PSMA-positive) was supplied from ATCC® (USA). The cells were cultured at 85% humidity, 5% CO_2, and 37 °C, in Dulbecco's Modified Eagle's Medium (DMEM; ATCC®; Atlanta, USA),10% fetal bovine serum, 100 μg/mL of streptomycin and 100 units/mL of penicillin.

2.5.2. Cell-binding affinity

A saturation binding assay was used to determine the affinity of purified $^{177}Lu_2O_3$-iPSMA NPs. A cellular suspension, at a density of 1×10^6 cells, was seeded in a 6-well plate and grown for 24 h to allow adherence (37 °C, 5% CO_2, and 85% humidity). The cells were placed on ice for 30 min. Afterward, the cells were incubated with seven different concentrations ($n = 3$) of the $^{177}Lu_2O_3$-iPSMA NPs (90 nM to 0.25 nM/200 μL) for 2 h at 4 °C. The non-specific binding was determined in parallel by the addition of "cold peptide" (iPSMA, 1 mol/L). Subsequently, the free (supernatant) and bound (attached and internalized to cells) radiopharmaceutical fractions were measured in a NaI (Tl) detector-equipped gamma counter (MNL Inc., Texas, USA) and analyzed based on standard solutions, representing 100% of the initial activity for each treatment. Specific binding was evaluated as the difference between non-specific binding and total binding. K_d and B_{max} were determined by non-linear regression analysis (GraphPad Prism software).

2.5.3. Cell internalization

$^{177}Lu_2O_3$ NP and $^{177}Lu_2O_3$-iPSMA NP internalization by HepG2 cells were evaluated using cell suspensions (4×10^5 cells/PBS) placed in test tubes (500 μL/tube). The cells were incubated at different times (0.5, 3, and 24 h), with 50 μL of each treatment ($n = 3$): a) $^{177}Lu_2O_3$ NPs (37 kBq), b) $^{177}Lu_2O_3$-iPSMA NPs (37 kBq), and c) no treatment (control). After the incubation period, the different fractions were measured in a NaI (Tl) detector-equipped gamma counter (MNL Inc., USA). The initial activity (total volume of the test tube) represented 100%. The samples were centrifuged (700*g*/5 min), the bottom portions were incubated with 1 M NaOH, centrifuged (700*g*/5 min), and the supernatant was collected and used to calculate the cellular internalization percentages.

2.5.4. Cell viability assay

For cell viability, the XTT (2,3-bis[2-methoxy-4-nitro-5-sulfophenyl]-2*H*-tetrazolium-5-caboxyanilide inner salt) assay was carried out. HepG2 cells, at a density of 1×10^4 cells/well, were seeded in a 96-well microplate (Corning, NY, USA) and incubated for 24 h (37 °C, 5% CO_2, and 85% humidity).

After overnight incubation, the medium was eliminated, and the cells were incubated for 1 h with the following treatments ($n = 3$): a) $^{177}Lu_2O_3$ NPs (37 kBq), b) $^{177}Lu_2O_3$-iPSMA (37 kBq) NPs and c) no treatment (control). Afterward, the treatments were removed, and the cells were washed twice with PBS; then, growth medium was added, and the microplates were incubated for 72 h (37 °C, 5% CO_2, and 85% humidity). Next, 100 μL of PBS and 50 μL of XTT (XTT kit, Roche Diagnostics GmbH; Mannheim, Germany) were added, and the cells were incubated for 4 h in order to allow the conversion of XTT to formazan (orange-colored dye) by the viable cells. The absorbance (at 450 nm) was measured in a microplate reader (EPOCH; BioTek Instruments; Winooski, Vermont, USA), considering the untreated cells as 100% in order to obtain the cell viability percentages.

2.6. In vivo biodistribution

In vivo studies in mice (Balb-C, 6–7 weeks old and a weight of 18–20 g) were performed according to the *Ethical Rules and Regulations for the Care of Laboratory Animals* guidelines (062-ZOO-1999 Official Mexican Norm). Mice were injected with $^{177}Lu_2O_3$-iPSMA nanoparticles (100 μL, 74 MBq) into the tail vein and sacrificed at 0.5, 1.5, 3, and 24 h ($n = 3$ for each time point). The heart, lungs, liver, pancreas, spleen, kidney, and blood samples were obtained for activity measurement in a NaI(Tl) detector to determine the percentage of the injected dose per gram of tissue (%ID/g), regarding the total injected activity.

2.7. Optical image

Luminescence images of the nanoparticles were obtained after irradiation by using an optical image preclinical system (Bruker Preclinical Optical/Xray Imaging System *in-Vivo* XTREME equipment), without any emission filter to verify the radioluminescence and with emission filters of 535, 600, 700, 750, 790 and 830 nm to obtain the intensity spectrum in photons/second/mm^2 *vs.* wavelength. X-ray images of the vials were acquired to corroborate the position of the powder and the luminescence. With the same equipment, and to verify the *in vivo* $^{177}Lu_2O_3$-iPSMA NPs biodistribution, as well as the radioluminescent properties, X-ray and luminescence images were obtained (without emission filters) from the whole body of mice at 2 min, 120 min, and 24 h after $^{177}Lu_2O_3$-iPSMA NPs administration (74 MBq, 1.0 mg). Rodent images were acquired with animals anesthetized with oxygen and 2% isoflurane in the supine position.

In addition, the nanoparticle vials were photographed before and after neutron irradiation, and in the dark, to appreciate the differences in color and radioluminescence with the naked eye.

3. Results

3.1. Synthesis of Lu_2O_3 NPs

The synthesis method employed was an easy route to obtain the Lu_2O_3 NPs with the expected characteristics, according to that previously reported. Among the advantages of the precipitation-calcination process, the fact that the synthesis can be carried out under ambient conditions (pressure and temperature), with relative ease and in a short amount of time, is important [21]. Furthermore, it is a much more straightforward method, which avoids undesired by-products [22], being the precipitant species, the OH^- and the $CO_3{}^{-2}$ ions. However, despite these adequate characteristics, the process is also susceptible to double carbonate formation. The double carbonates are a phase unique to this methodology, where, regardless of the salt used, the final product is doubled [23]. For the methodology used, this double carbonate was the immediate precursor of the Lu_2O_3 NPs.The stoichiometry of the synthesis is summarized in the following equations (Eqs. (1)–(4)):

$$LuCl_3 \longrightarrow Lu^{+3} + 3Cl^{-1} \quad (1)$$

$$Lu^{+3} + 3Cl^{-1} + 3NH_4OH \longrightarrow Lu(OH)_3 + 3NH_4Cl \quad (2)$$

$$3Lu(OH)_3 + 4(NH_4)_2CO_3 + 2H_2O \longrightarrow Lu(OH)(CO_3)\bullet xH_2O + Lu_2(CO_3)_3 \bullet xH_2O + 6NH_4OH + 2NH_3 + 2H_2O \quad (3)$$

$$2Lu(OH)(CO_3)\bullet xH_2O + Lu_2(CO_3)_3\bullet xH_2O \longrightarrow 2Lu_2O_3 + 5CO_2 + 4H_2O \quad (4)$$

3.2. Physicochemical characterization

3.2.1. DSC-TGA analysis

The thermogravimetric analyses were performed with the raw material ($Lu(OH)(CO_3) \cdot xH_2O/Lu_2(CO_3)_3 \cdot xH_2O$) dried at 110 °C. Fig. 1 indicates the thermal behavior of the lutetium carbonate and lutetium hydroxycarbonate precursors; generally, rare-earth carbonates have three main stages: a) dehydration, b) partial decarbonation, and c) full decarbonation. In the first stage, a weight loss from 5% to 20% is expected and depends on the type of lanthanide [23]. This effect occurs below 100 °C, but also, crystalline water in the hydroxycarbonate is lost at a 200 °C–500 °C interval. Then, the carbonate partially decomposes into the oxycarbonate to finally decompose into the respective oxide.

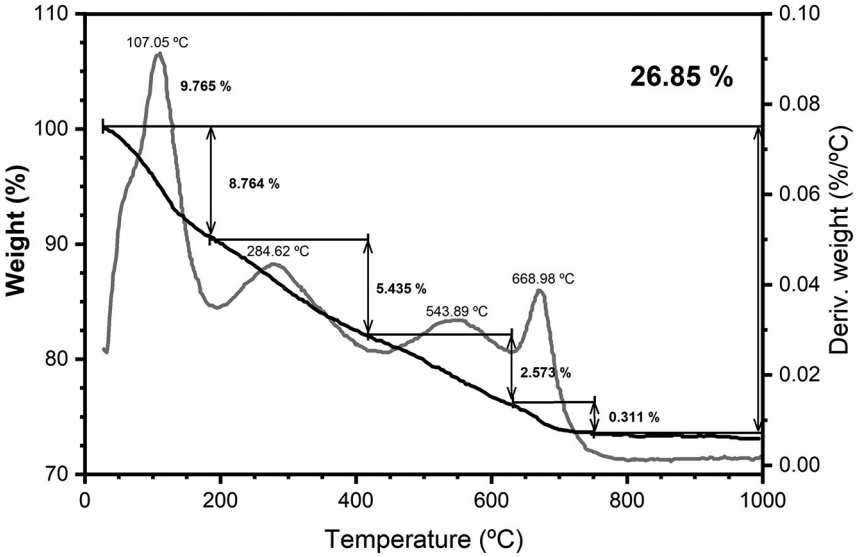

Fig. 1. DSC-TGA curves of the $Lu(OH)(CO_3) \cdot xH_2O/Lu_2(CO_3)_3 \cdot xH_2O$ precursors of Lu_2O_3 nanoparticle formation.

The obtained pattern of the lutetium carbonate showed the different weight loss stages, and a total weight loss of 26.85%, which agrees with that previously reported [23]. The weight loss below 100 °C is related to adsorbed water. Between 107 °C to 284 °C, the weight loss was mainly attributable to the decomposition of organic species (partial decarbonation), and above 668.98 °C, up to about 750 °C, another loss of mass is obtained attributed to full decarbonation [23,24]. According to the DSC-TGA analysis, the presence of hydrated species can be proposed. In agreement with the reagents employed, two compounds can be formed: lutetium carbonate ($Lu_2(CO_3)_3 \cdot xH_2O$) and lutetium hydroxycarbonate ($Lu(OH)(CO_3) \cdot xH_2O$). Both are formed simultaneously and correspond to the precipitate that is observed when a pH of 9 is reached (Eq. (3)), but with different modes of thermal decomposition. Nonetheless, both chemical species ultimately lead to the formation of Lu2O3. Eq. (3) can be further elaborated to give the following:

a) When the precursor is the hydroxycarbonate, the decomposition to lutetium oxide occurs in the following manner:

$$Lu(OH)(CO_3)\cdot xH_2O \longrightarrow Lu(OH)(CO_3) + xH_2O \quad (3.1.1)$$

Reaction 3.1.1 represents the first loss of water, which, in the thermogram, corresponds to the loss located at around 100 °C.

$$2\,Lu(OH)(CO_3) \longrightarrow Lu_2O_2(CO_3) + CO_2 + H_2O \quad (3.1.2)$$

Reaction 3.1.2 represents the first decarboxylation and the loss of water that continues at temperatures above 100 °C.

$$Lu_2O_2(CO_3) \rightarrow Lu_2O_3 + CO_2 \quad (3.1.3)$$

Reaction 3.1.3 represents the second decarboxylation and the complete formation of lutetium oxide. It occurs at around 600 °C, and no mass-loss ramp is observed in the thermogram.

b) When the precursor is the carbonate, the decomposition to lutetium oxide is as follows:

$$Lu_2(CO_3)_3\cdot xH_2O \longrightarrow Lu_2(CO_3)_3 + xH_2O \quad (3.2.1)$$

As with the hydroxycarbonate, reaction 3.2.1 represents the first loss of water, which is seen at around 100 °C.

$$Lu_2(CO_3)_3 \longrightarrow Lu_2O_2(CO_3) + 2CO_2 \quad (3.2.2)$$

Reaction 3.2.2 is the first decarboxylation

$$Lu_2O_2(CO_3) \rightarrow Lu_2O_3 + CO_2 \quad (3.2.3)$$

Reaction 3.2.3 represents the second decarboxylation and complete calcination to Lu2O3 at a temperature above 600 °C.

3.2.2. Size and morphology

The resulting nanoparticles were a fine and fluffy powder. TEM studies revealed the presence of particles with a structure close to a spherical form and with homogeneous and uniform distribution. The SEM images exhibited homogeneity in the material's morphology. The mean diameter obtained for Lu_2O_3 NPs and determined by TEM was 26.75 nm ± 6.72 nm, with a monomodal and monodisperse distribution, as is shown in Fig. 2a–c.

After the Lu_2O_3 NPs were functionalized with the peptide, the system showed an increase of ~3 nm, with a mean diameter of 29.98 nm ± 9.07 nm and maintaining a homogeneous size distribution, which is seen in the monomodal and monodisperse histogram. Additionally, in the TEM micrographs, it was possible to observe that the precursor still retained the morphology and that the peptide was present at the surface of the nanoparticles, with a width of ~2.7 nm, as is shown in Fig. 3a–c.

3.2.3. DLS and zeta potential

DLS measured the mean hydrodynamic diameter, and Lu_2O_3 NPs sizes were 107.43 nm ± 33.78 nm. After the functionalization with iPSMA, an increase in the mean hydrodynamic diameter (177.75 nm ± 57.51 nm) and the polydispersity index (PDI) was observed, which is attributed to the presence of the peptide in the nanosystem structure. All samples showed monomodal and monodisperse distributions. As expected, in both cases (NPs with and without peptide), the hydrodynamic nanoparticle sizes were higher than those of the diameters determined by TEM, since measurement techniques are different in terms of physical principles.

Zeta potential (ζ) values increased when the peptide was incorporated over the nanoparticle surface; for Lu_2O_3 NPs, the value was −27.40 mV, and for Lu_2O_3-iPSMA, it was −44.55 mV. This difference was attributed to the correct synthesis of the functionalized system. The mean hydrodynamic diameter distributions and ζ measurements are summarized in Table 1.

3.2.4. Identity, purity, and crystallinity

HRTEM micrographs showed the highly crystalline Lu_2O_3 nanoparticles with the lattice fringes, corresponding to the (222) plane of the lanthanide crystal, with a lattice spacing of 0.299 nm (Fig. 4a). Furthermore, evidence of the identity, purity, and crystal structure was verified by the Selected Area Electron Diffraction pattern (Fig. 4b),

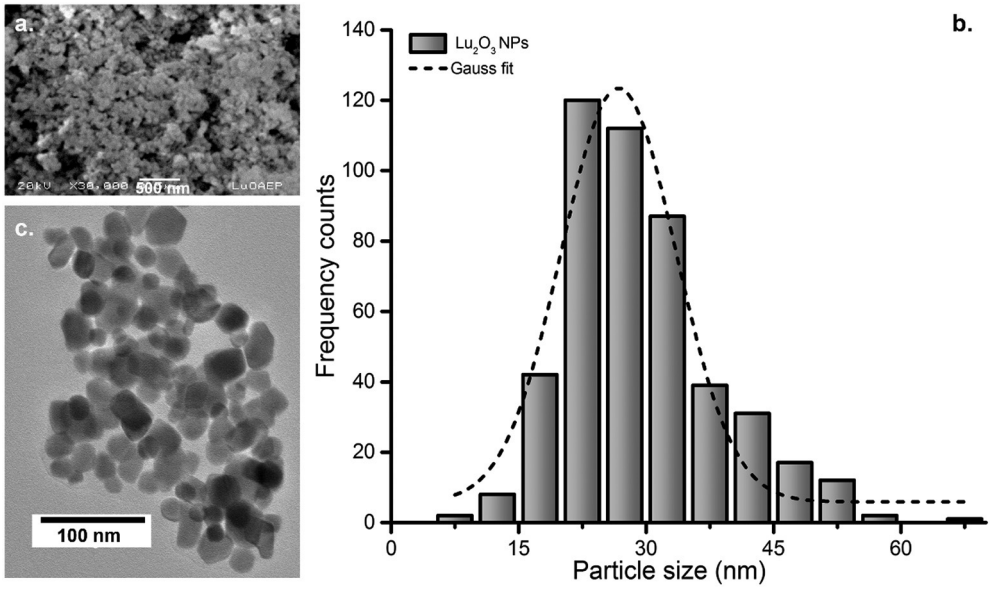

Fig. 2. a) SEM micrographs of Lu_2O_3, b) size distribution of Lu_2O_3 by TEM and c) TEM micrographs of Lu_2O_3 NPs.

where Lu_2O_3 was identified as having a cubic fluorite-type phase, belonging to the space group *Ia3* [25], as identified by the JCPDS card No. 12–0728 (a = 10.3900), which also coincided with the X-Ray Powder Diffraction results (Fig. 4c), with the major characteristic peaks for the lanthanide oxide, at 2θ values of 20.749° (211), 29.629° (222), 34.365° (400), 35.565° (411), 40.568° (332), 44.233° (431), 49.464° (440), 54.236° (611), 57.375° (541), 58.761° (622), 60.278° (631), 61.278° (444), 65.931° (217), 71.286° (651), 72.591° (800), 74.002° (741), 79.187° (831), 80.411° (662), and 82.939° (840). Moreover, the XRD spectra showed well-defined and narrow peaks, indicative of the crystallinity and purity of the material.

With the information from the XRD pattern, the mean particle diameter was also calculated employing the Scherrer equation (Eq. (5)), and according to the value of the (2 2 2) plane refraction peak, which was used as a reference peak width at angle θ = 29.629°.

Table 1
Hydrodynamic diameter, PDI, and zeta potential of Lu_2O_3 NPs and Lu_2O_3-iPSMA NPs.

Nanoparticle system	Hydrodynamic diameter (nm)	PDI	ζ (mV)
Lu_2O_3 NPs	107.43 nm ± 33.78 nm	0.1249	−27.40
Lu_2O_3-iPSMA NPs	177.75 nm ± 57.51 nm	0.3423	−44.55

$$D = \frac{K\lambda}{\beta\cos\theta} \tag{5}$$

where D is the particle size calculated, λ is the X-ray wavelength of the CuKα source (0.15406 nm), β is the full width at half the maximum of the central peak (FWHM), K is the shape factor of the unit cell, and θ is the Bragg angle. The theoretical value was ~30.01 nm, which agrees

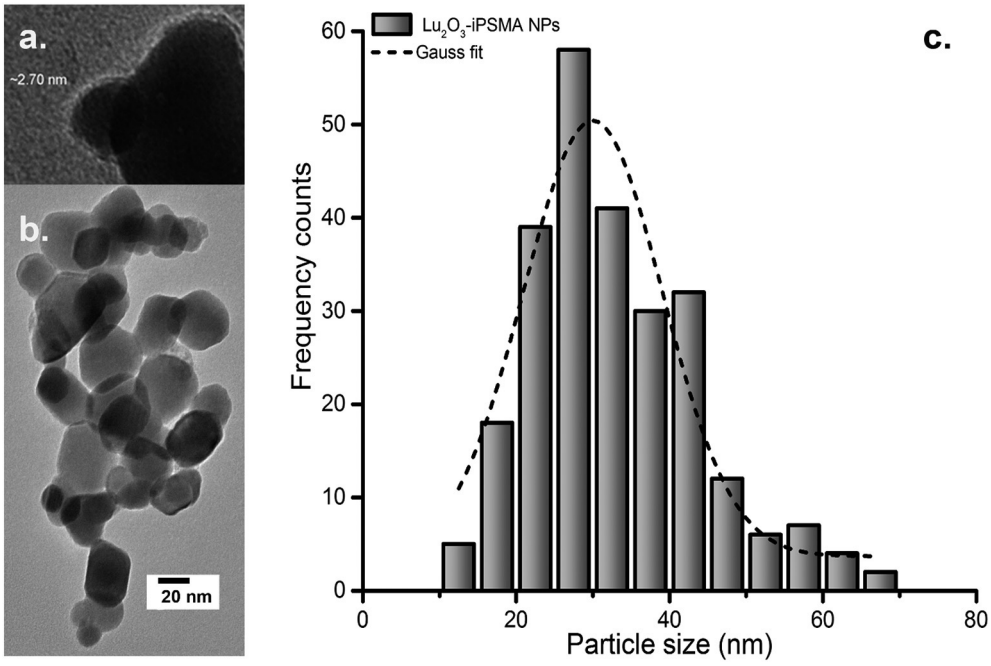

Fig. 3. a) Close-up of the iPSMA peptide attached at the Lu_2O_3 NP surface, b) TEM micrograph of Lu_2O_3-iPSMA NPs, and c) size distribution of Lu_2O_3-iPSMA NPs.

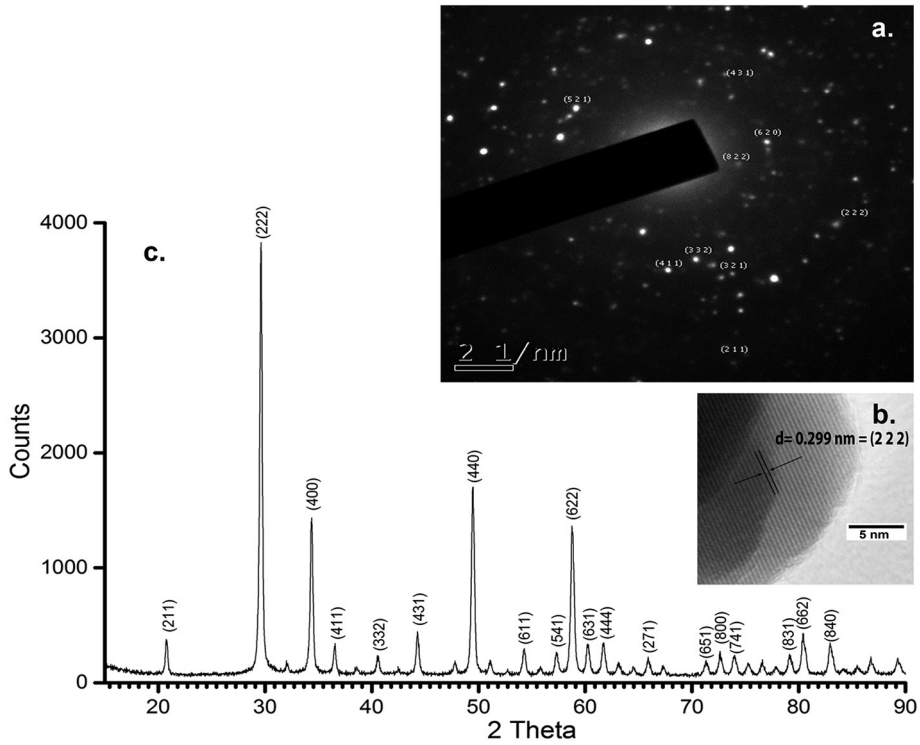

Fig. 4. Crystallinity parameters of Lu_2O_3 NPs by a) HRTEM, b) SAED, and c) XRD of powders.

with the value obtained by TEM.

3.3. Surface functionalization

3.3.1. FT-IR spectroscopy

The MIR spectra of the Lu_2O_3 NPs, Lu_2O_3-iPSMA NPs, and DOTA-HYNIC-iPSMA (iPSMA) are given in Fig. 5. All the spectra were highly structured.

Lu_2O_3 NPs spectrum: a vibration band formed at 574 cm^{-1} corresponds to the stretching vibration of Lu—O, and it is also indicative of both the nanometric size and the complete crystallization to lutetium oxide [26].

Lu_2O_3-iPSMA spectrum: the vibration band at 3362 cm^{-1} was assigned to the vibration of the N—H group from the amide. The typical

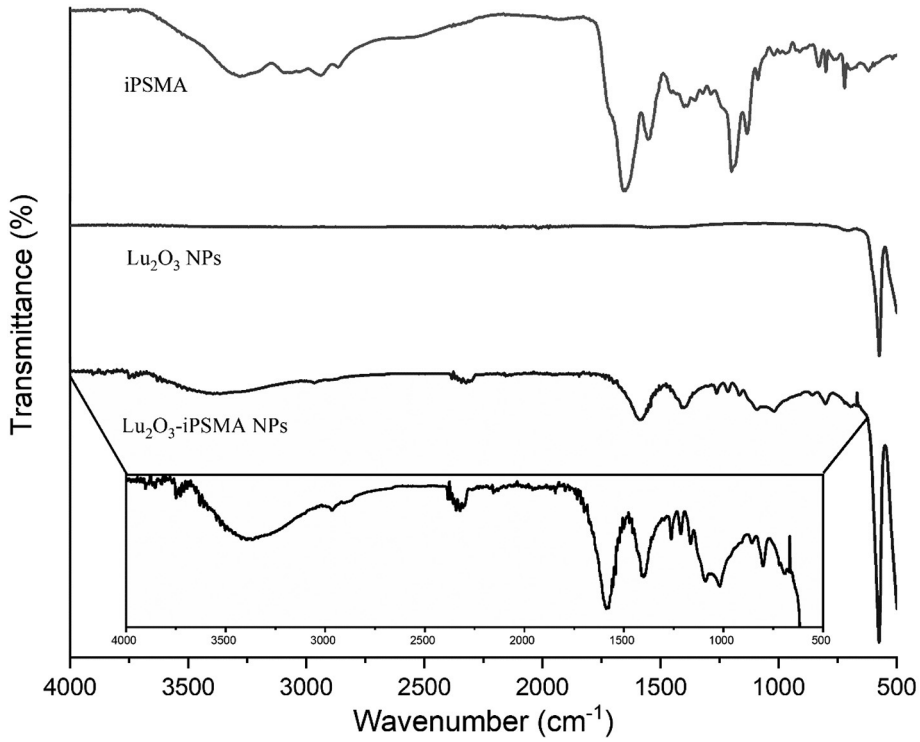

Fig. 5. Medium infrared spectra of iPSMA, Lu_2O_3 NPs, and Lu_2O_3-iPSMA NPs, the latter with an inset for IR spectrum amplification.

Table 2
FT-IR vibrational bands of the iPSMA peptide, Lu_2O_3 NPs, and Lu_2O_3-iPSMA NPs.

Vibration	Wavenumber (cm^{-1})		
	DOTA-HYNIC-iPSMA (iPSMA)	Lu_2O_3 NPs	Lu_2O_3-iPSMA NPs
ν N-H	3281	–	3362
νas–CH_2-	2938	–	2964
νs–CH_2-	2863	–	2885
O-H (-COOH)	2537	–	2343
νsC=O	1652	–	1588
N-H (urea) -C-N C=C	1551	–	1420
Phe ring νC-C	1442–1347	–	1400–1214
ν N–N (in-plane) (HYNIC)	1321–1133	–	1116–1018
ν C–H (out-of-plane) (HYNIC)	967–830	–	856–691
δ -CH_2-	720	–	–
δ N-C=O	621	–	–
δ C=H	479	–	–
ν Lu-O	–	575	571

vibrational bands for the methyl and methylene groups of the aliphatic chain (v_{as} and v_s stretching) were assigned at 2964 cm^{-1} and 2885 cm^{-1}, respectively. At 2343 cm^{-1}, the vibration band was assigned to the O–H vibration from the -COOH groups of the DOTA moiety. The strong stretching band at 1588 cm^{-1} was assigned to the C=O groups present in the final compound. In the region between 1588 cm^{-1}–1420 cm^{-1}, the vibrations of the –N-H, C=C, and C–N groups were observed. The typical stretching vibration of the –C-N from the urea group of the iPSMA moiety had a band at 1409 cm^{-1}. The C-N-C vibrations from the DOTA structure appeared between 1239 cm^{-1} to 1161 cm^{-1}, and the δ vibrations of the C–H (out-of-plane) were present between 856 cm^{-1} and 691 cm^{-1}. Finally, the band from the metal stretching vibration appeared at 576 cm^{-1} [14,20].

It is important to highlight that all the vibration bands just described showed a significant displacement (~50 cm^{-1} to 70 cm^{-1}) compared to the iPSMA spectrum. Also, the spectrum of the bare Lu_2O_3 NPs showed no other band besides the one that corresponds to the Lu–O vibration. The results of FT-IR are summarized in Table 2.

3.3.2. UV–Vis spectroscopy

UV–Vis spectra showed an adequate functionalization of Lu_2O_3 nanoparticles, for which the spectrum of the Lu_2O_3-iPSMA NPs showed an absorption band centered at 216 nm, in addition to a shoulder that overlaps this band at around 226 nm. The first absorption band turned out to be characteristic of the bare Lu_2O_3 NPs, corresponding to the chemical structure of the material with the form Lu_2O_3, where Lu^{+3} represents the lanthanide ion and O refers to the O^{-2} ion, which is also indicative of the nanometer size of the oxide, as previously reported [21,27].

Additionally, the second band was associated with the presence of the peptide on the nanoparticle surface [14], more specifically due to the carboxylic acids from the DOTA group of the said molecule [28]. Both bands in the functionalized system exhibited a slight blue shift of approximately 3 nm, further indicating a change in the chemical environment (Fig. 6).

3.4. Physicochemical evaluation of Lu_2O_3 NPs after neutron activation

After irradiation of $^{nat}Lu_2O_3$ NPs (100 mg), the obtained activity was 7.81 GBq. Morphology, size, chemical composition, and stability of the irradiated nanoparticles were evaluated after 6 months of radioactive decay to determine if the physicochemical properties of the nanomaterial had not changed.

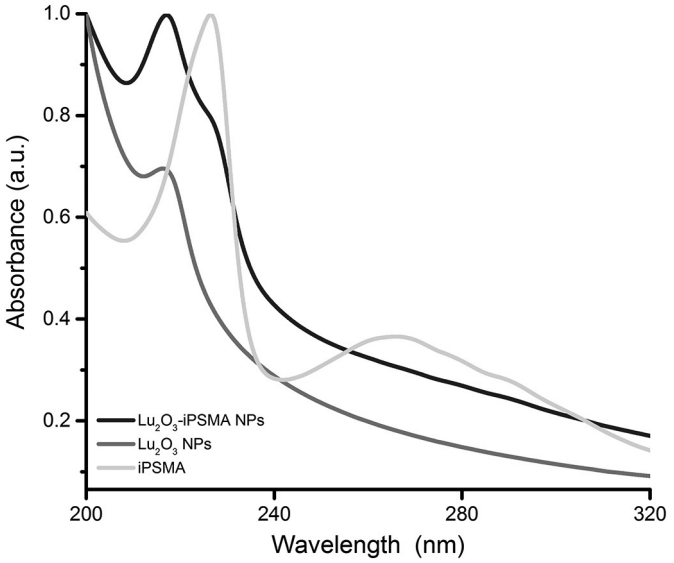

Fig. 6. UV–Vis spectra of Lu_2O_3 NPs, Lu_2O_3-iPSMA conjugate, and DOTA-HYNIC-iPSMA (iPSMA) peptide solution.

TEM images showed that a spherical morphology was retained by the material, as well as the uniform and homogeneous distribution. The average diameter obtained from the measurements of ~700 particles was 30.12 nm ± 10.12 nm, with a distinctive histogram of a monomodal and monodisperse population. The hydrodynamic diameter (DLS) was 93 nm ± 34 nm (PDI = 0.2402), also with a monomodal and monodisperse distribution. Another parameter that kept its conditions was the zeta potential, with a value of −41 mV. Finally, the FT-IR spectra showed no changes, where the bands correlated to the lutetium and peptide vibrations were kept. These results showed that the main physicochemical properties of the material were adequately maintained and without significant changes after being activated to its corresponding radionuclide.

3.5. Biochemical characterization, biodistribution and in vivo imaging

The saturation binding study of $^{177}Lu_2O_3$-iPSMA NPs on PSMA-positive HepG2 cells is shown in Fig. 7. Affinity data with a K_d = 5.7 ± 1.9 nM and B_{max} = 1.6 ± 0.1 nM indicate that the nanoparticles conjugated to the peptide exhibited a good biological affinity for PSMA receptors.

The cytotoxicity results correlated with the cell uptake data. A reduction in the viability of HepG2 cells, dependent on the recognition mediated by the specific receptor PSMA, was observed. Cells treated with $^{177}Lu_2O_3$-iPSMA NPs (72 h after treatment) showed 53.48 ± 2.58% of viability with a statistically significant difference ($p < .05$, Student's t-test) with regard to the group treated with $^{177}Lu_2O_3$ NPs (68.79 ± 2.27%). The decrease in viability, because of the treatment with $^{177}Lu_2O_3$ NPs, is attributed to the non-specific uptake of radiolabeled nanoparticles and the crossfire effect produced by radiation in the medium. The biodistribution profile of the nanosystem in healthy mice showed the main uptake in spleen and liver (Table 3). After irradiation, radioactive Lu_2O_3-iPSMA NPs exhibited radioluminescent properties, making the *in vivo* acquisition of their biodistribution, *via* optical imaging, possible (Figs. 9 and 10).

4. Discussion

Lutetium oxide nanoparticles were successfully synthesized; its quasi-spherical morphology, crystal structure [21,25], particle size (26.75 nm ± 6.72 nm), colloidal stability (ζ = −27.40 eV) and

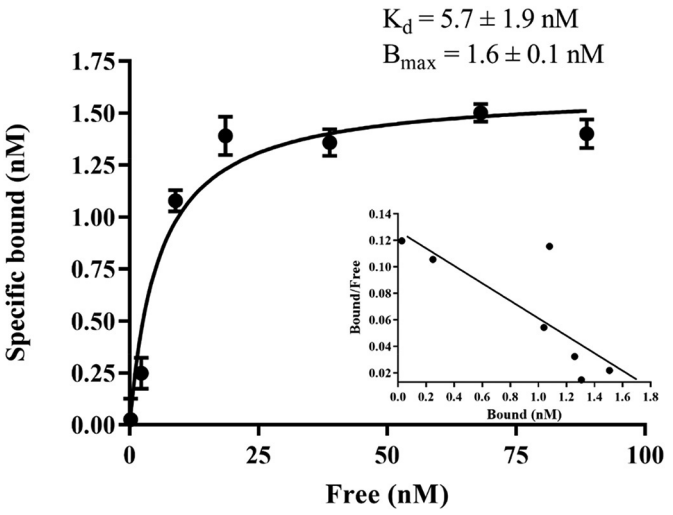

Fig. 7. Saturation binding assay of $^{177}Lu_2O_3$-iPSMA NPs on PSMA-positive HepG2 cells. Cellular internalization studies exhibited a statistically higher internalization of $^{177}Lu_2O_3$-iPSMA NPs, compared to the $^{177}Lu_2O_3$ NPs in HepG2 cells at different times (Fig. 8).

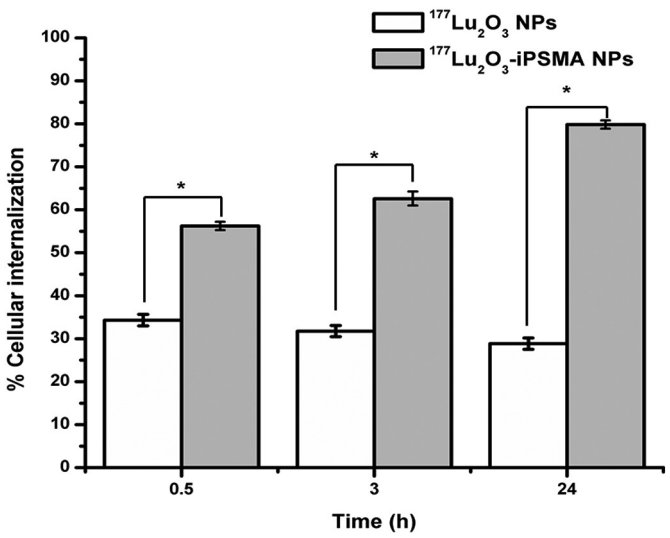

Fig. 8. Internalization of $^{177}Lu_2O_3$ NPs and $^{177}Lu_2O_3$-iPSMA NPs at different times in PSMA-positive HepG2 cells (*statistically significant difference: $p < .05$, Student's *t*-test.).

Table 3
Biodistribution of $^{177}Lu_2O_3$-iPSMA nanoparticles in healthy mice (Balb-C), stated as a percentage of radioactivity per gram of tissue (% ID/g) at different times (mean ± SD, $n = 3$).

Tissue	Time (h)			
	0.5	3	24	96
Blood	1.48 ± 0.32	0.74 ± 0.21	0.19 ± 0.08	0.08 ± 0.04
Heart	1.03 ± 0.27	0.55 ± 0.19	0.22 ± 0.14	0.11 ± 0.07
Lung	2.14 ± 0.82	1.02 ± 0.31	0.57 ± 0.15	0.38 ± 0.05
Liver	11.42 ± 1.73	10.94 ± 1.42	8.87 ± 1.03	3.72 ± 0.83
Pancreas	0.54 ± 0.23	0.59 ± 0.19	0.27 ± 0.11	0.18 ± 0.08
Spleen	2.41 ± 0.93	1.13 ± 0.71	0.81 ± 0.67	0.72 ± 0.59
Kidney	3.85 ± 0.88	2.08 ± 0.82	0.71 ± 0.33	0.58 ± 0.12

chemical composition were verified with the appropriate analytical techniques.

The FT-IR spectrum of the bare material showed the characteristic stretching band of the Lu_2O_3 NPs, which was also correlated to adequate crystallization. On the other hand, the oxide nanoparticles were properly functionalized with the DOTA-HYNIC-iPSMA peptide sequence, due to the strong coordination capability of Lu ions that were free at the material's surface, facilitating the formation of the complex with molecules comprising groups such as –COOH. In this specific case, the conjugation was carried out with –COOH groups from DOTA and with the Lu^{3+} ions exposed on the nanoparticle surface. Moreover, the vibrational bands of –COOH groups can be used to determine the interaction between the carboxylate head and the metal ions [23,29]. Additionally, the UV–Vis spectra bands showed the presence of the peptide in the final system, as well as in the TEM images. Zeta potential increased 17 units after functionalization due to the presence of the peptide itself, which, in turn, enhanced the stability of the Lu_2O_3-iPSMA NPs. The mean size of the Lu_2O_3-iPSMA NPs was about 29 nm ± 9 nm, a similar value to that obtained theoretically and experimentally, which is an essential requirement for the nanosystems, since it has been proven that sizes < 50 nm improve the processes of uptake and internalization at the cellular level [10,30]. The results showed that a high internalization occurred in the functionalized system ($^{177}Lu_2O_3$-iPSMA NPs), indicating a specific recognition by HepG2 cells. The observed $^{177}Lu_2O_3$ NPs internalization is in the range of other nanosystems due to a passive mechanism uptake [13]. However, $^{177}Lu_2O_3$ NPs had a significant lower internalization with respect to $^{177}Lu_2O_3$-iPSMA NPs, which is attributable to the absence of the peptide in their structure (Fig. 8). The internalization of $^{177}Lu_2O3$ NPs decreased when the incubation time increased (from 35% to 28%) (Fig. 8). This behavior can be attributed to the nanoparticle size [31]. $^{177}Lu_2O_3$ NPs are less than 50 nm in size, and, in the absence of specific recognition biomolecules on their surface, the nanoparticles showed a significant outflow from cells.

The saturation binding assay was used to determine the nanosystem affinity. Nanoparticles conjugated to the peptide showed a suitable affinity for PSMA ($^{177}Lu_2O_3$-iPSMA NPs

$K_d = 5.7 \pm 1.9$ nM, Bmax = 1.6 ± 0.1 nM). These results indicate that although the iPSMA molecules are linked to the lutetium oxide nanoparticles, their active sites for binding with their respective receptor (PSMA) in cells are not significantly affected, which is in agreement with previous reports where iPSMA has also been conjugated to different molecules through the DOTA complex [14,16,17], or by binding peptides to different nanoparticles [15]. $^{177}Lu_2O_3$-iPSMA NPs show a high and selective binding to HepG2 cells that overexpress PSMA and, due to affinity is a critical parameter that significantly influences the uptake by the tumor, the $^{177}Lu_2O_3$-iPSMA nanoparticulate system has the potential to be used as a target-specific theranostic agent [32]. The therapeutic potential was also corroborated by the cytotoxic effect of the radionanoparticles on the HepG2 cells, which was significantly higher at 72 h after $^{177}Lu_2O_3$-iPSMA NPs treatment (53.48% of viability) with regard to the $^{177}Lu_2O_3$ NPs treatment (69.79% of viability). At this point, it is relevant to emphasize that in assays performed at an *in vitro* level, all nanoparticles have a high non-specific cell uptake due to a passive mechanism [13]. However, it is expected that the *in vivo* uptake and internalization at the cellular level of non-functionalized nanoparticles be much lower than that observed *in vitro* [13,33].

Biodistribution data demonstrated that most of the nanoparticles accumulated in the liver (Table 3). It is pertinent to underline that liver cancer overexpresses the PSMA

protein [34–36] and, considering that hepatic radioembolization treatment for this type of tumors is indicated when tumoral lesions have compromised two-thirds of hepatic tissue, $^{177}Lu_2O_3$-iPSMA NPs could have potential to be used as specific agents in targeted radiotherapy. Nonetheless, it would be necessary to evaluate this new nanosystem in mice with orthotopic hepatic tumors using cells different from the HepG2 cells employed for this research, since these do not develop tumors in preclinical murine models. In the case of radioembolization

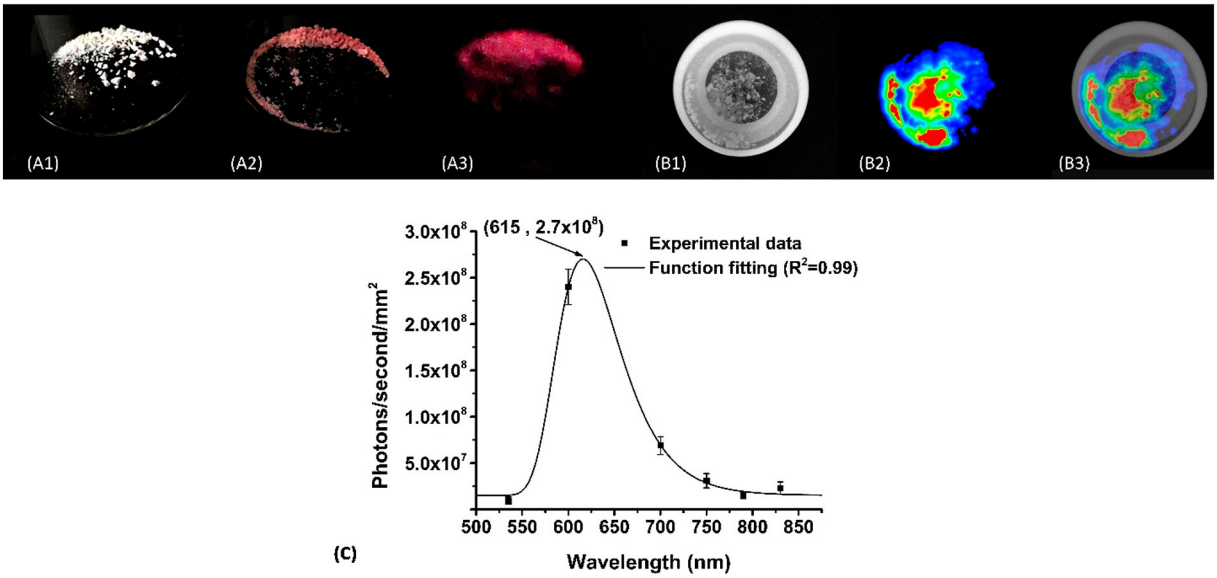

Fig. 9. A) $^{177}Lu_2O_3$-iPSMA nanoparticles (powder) before (A1) and after (A2) neutron irradiation, and their radioluminescence (A3) in a dark room. B) $^{177}Lu_2O_3$-iPSMA nanoparticles (powder): X-ray image (B1), luminescent image (B2), and merged images (B3). C) $^{177}Lu_2O_3$-iPSMA nanoparticle (powder) emission spectrum.

for hepatocellular carcinoma therapy, ^{90}Y-glass microspheres (size of 20–30 μm) are commonly employed to obstruct the hepatic artery and produce a tumoral brachytherapy system [37,38]. The advantage of the $^{177}Lu_2O_3$-iPSMA nanosystem (< 50 nm) would be its targeted internalization into tumor cells to deliver a maximum radiation dose in a selective and localized manner. However, it is essential to clarify that the application of nanoparticles would not be limited to hepatocellular carcinoma, but also to any tumor that overexpresses the PSMA protein, evaluating in each therapeutic application, the route of administration (*e.g.*, intratumorally, intra-arterially, *etc.*) to optimize the radiation dose to tumors.

After neutron activation, the $^{177}Lu_2O_3$ and $^{177}Lu_2O_3$-iPSMA nanoparticles showed radioluminescence properties due to the interaction of the material with ionizing radiation, establishing a possible biological application for obtaining preclinical optical imaging. The importance of using lanthanides for imaging lies in their long luminescence half-life. In lanthanides, this property is associated with the electronic structure of trivalent ions, related explicitly to intra-configurations within its 4*f* orbital (*f-f* transitions), as well as to the protective effect provided by the electrons of the $5s^2$ and $5p^6$ levels (full), which do not allow disturbances of the surrounding environment. In addition, these intra-configurational changes do not generate inverse modifications either; that is, they do not alter the chemical bonds that the compound may form [39–41], allowing an extended emission (like-linear emission), with narrow and characteristic bands in the UV–Vis and near-infrared range, associated with a unique color for each material [42]. Another way of producing the excitation of the nanoparticles (specifically of their Lu^{3+} ions) is indirectly by the organic ligands present in their composition, which when excited to their singlet state, can produce intramolecular energy transfer to the lanthanide ions, causing indirect excitation in the trivalent ion, which emits this energy linearly towards a lower 4*f* state [41]. Therefore, these ligands would fulfill two essential functions: improvement in the biological properties, as well as in the luminescent properties of the system.

It is important to highlight that the luminescence photonic emission effect is enhanced in the lutetium nanoparticles by the large surface area on these scales, allowing for higher absorption coefficients, reflected in three main characteristics: a) easily-recognizable spectra, b) linear emission spectra, and c) longer lifetimes with high resistance to photobleaching. In addition to the above, the nanometric size allows greater mobility of Lu^{3+} ions, which, due to the proximity between them, improve and contribute to the transfer of ion-ion energy, allowing an energy movement constant even without the presence of organic molecules, thus, the desired effect is produced. It can be explained by the up-conversion phenomenon, either by the mechanism based on the conversion energy transfer between two neighboring ions (ETU) or by the photon avalanche (PA), which are mechanisms involving two neighboring ions. However, the ETU mechanism is the most feasible and efficient [8,43,44].

5. Conclusions

In this study, the nanoparticle $^{177}Lu_2O_3$-iPSMA system was prepared and evaluated as a potential targeted therapy agent. The results showed excellent physicochemical properties that allowed the nanosystem to be activated by neutron irradiation for biological assessment and optical *in*

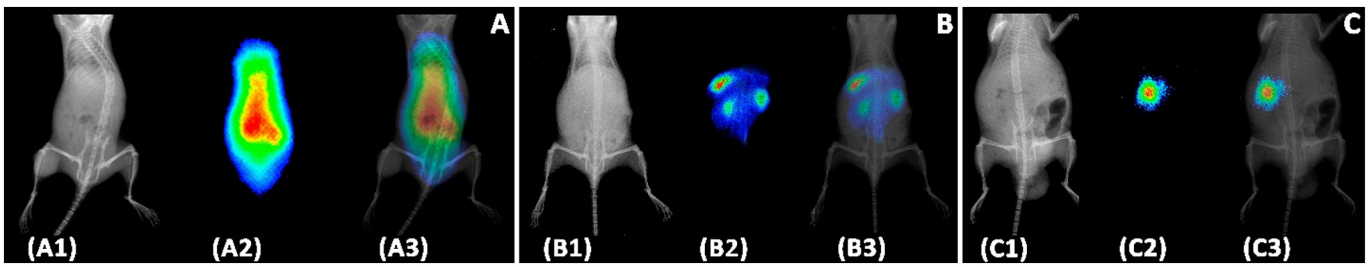

Fig. 10. Biodistribution in mice of $^{177}Lu_2O_3$-iPSMA nanoparticles (74 MBq, 1.0 mg) at 2 min (A), 120 min (B) and 24 h (C) after administration: X-ray images (A1, B1, C1), luminescent image (A2, B2, C2), and merged images (A3, B3, C3).

vivo imaging. The *in vitro* studies indicated a good $^{177}Lu_2O_3$-iPSMA affinity to cells overexpressing PSMA. The results obtained from this research support the execution of additional preclinical studies with the objective of evaluating the dosimetry and therapeutic efficacy of the $^{177}Lu_2O_3$ iPSMA nanoparticles for the *in vivo* imaging (nuclear and optical) and targeted radiotherapy of tumors overexpressing the PSMA protein.

Funding statement

This study was supported by the Mexican National Council of Science and Technology (CONACyT) grant CB2017-2018-A1-S-36841.

Authors' individual contributions

Ancira-Cortez A: Performed most of the experimental studies and data analysis and interpretation. Contributor in writing the manuscript

Ferro-Flores G.: Conception and design of the study. Data analysis and interpretation. The major contributors in writing and editing the manuscript.

Jiménez-Mancilla N.: Design of the study. Final revision of the manuscript and enhancement of its intellectual content.

Morales-Avila E.: Synthesis design. Data analysis of chemical characterization.

Trujillo-Benítez D: Preparation and purification of functionalized nanoparticles.

Ocampo-García B: Biochemical characterization: internalization and viability assays and cytotoxic evaluation.

Santos-Cuevas C.: Biodistribution studies and *in vivo* optical imaging acquisition.

Escudero-Castellanos A.: Biochemical characterization: binding and affinity assays.

Luna-Gutiérrez M.: Radiochemical data acquisition, data analysis and interpretation.

All authors read and approved the final manuscript.

Declaration of competing interest

The authors declare that they have no known competing financial interests or personal relationships that could have appeared to influence the work reported in this paper.

Acknowledgments

This study was conducted as a component of the activities of the "Laboratorio Nacional de Investigación y Desarrollo de Radiofármacos, CONACyT" (LANIDER).

References

[1] C. Dhand, et al., Methods and strategies for the synthesis of diverse nanoparticles and their applications: a comprehensive overview, RSC Adv. 5 (127) (2015) 105003–105037, https://doi.org/10.1039/c5ra19388e.

[2] P. Aryanrad, et al., Europium oxide nanorod-reduced graphene oxide nanocomposites towards supercapacitors, RSC Adv. 10 (30) (2020) 17543–17551, https://doi.org/10.1039/c9ra11012g.

[3] Y. Yu, et al., Enhanced photothermal conversion performances with ultra-broad plasmon absorption of Au in Au/Sm_2O_3 composites, J. Am. Ceram. Soc. (2020), https://doi.org/10.1111/jace.17133.

[4] J.L. Mason, et al., Exceptionally complex electronic structures of lanthanide oxides and small molecules, Acc. Chem. Res. 52 (11) (2019) 3265–3273, https://doi.org/10.1021/acs.accounts.9b00474.

[5] S. Banerjee, M.R. Pillai, F.F. Knapp, Lutetium-177 therapeutic radiopharmaceuticals: linking chemistry, radiochemistry, and practical applications, Chem. Rev. 115 (8) (2015) 2934–2974, https://doi.org/10.1021/cr500171e.

[6] M. Rahimi-Nasrabadi, et al., Optimized synthesis and characterization of lutetium carbonate and oxide nanoparticles and their use as degradation photocatalyst, J. Mater. Sci. Mater. Electron. 28 (22) (2017) 17078–17088, https://doi.org/10.1007/s10854-017-7634-7.

[7] K. Huang, M.K.G. Jayakumar, Y. Zhang, Lutetium doping for making big core and core-shell upconversion nanoparticles, J. Mater. Chem. C 3 (39) (2015) 10267–10272, https://doi.org/10.1039/c5tc00817d.

[8] Z. Gerelkhuu, et al., One-step synthesis of NaLu80-xGdxF4: Yb183+/Er23+(Tm3+) upconversion nanoparticles for in vitro cell imaging, Mater. Sci. Eng. C Mater. Biol. Appl. 86 (2018) 56–61, https://doi.org/10.1016/j.msec.2017.11.019.

[9] T. Ahmad, I.H. Lone, Development of multifunctional lutetium ferrite nanoparticles: structural characterization and properties, Mat Chem Phys 202 (2017) 50–55, https://doi.org/10.1016/j.matchemphys.2017.08.068.

[10] C.H. Yeong, et al., Therapeutic radionuclides in nuclear medicine: current and future prospects, J Zhejiang Univ Sci B 15 (10) (2014) 845–863, https://doi.org/10.1631/jzus.B1400131.

[11] A.M. Pillai, F.F. Knapp, Evolving important role of Lutetium-177 for therapeutic nuclear medicine, Curr. Radiopharm. 8 (2) (2015) 78–85, https://doi.org/10.2174/1874471008666150312155959.

[12] J. You, et al., Chemoradiation therapy using cyclopamine-loaded liquid-lipid nanoparticles and Lutetium-177-labeled core-crosslinked polymeric micelles, J. Control. Release 202 (2015) 40–48, https://doi.org/10.1016/j.jconrel.2015.01.031.

[13] A. Vilchis-Juarez, et al., Molecular targeting radiotherapy with cyclo-RGDFK(C) peptides conjugated to ^{177}Lu-labeled gold nanoparticles in tumor-bearing mice, J Biomed Nanotechnol 1 (0(3)) (2014) 393–404, https://doi.org/10.1166/jbn.2014.1721.

[14] A. Escudero-Castellanos, et al., Preparation and in vitro evaluation of ^{177}Lu-iPSMA-RGD as a new heterobivalent radiopharmaceutical, J. Radioanal. Nucl. Chem. 314 (3) (2017) 2201–2207, https://doi.org/10.1007/s10967-017-5555-9.

[15] T. Liu, et al., Targeting prostate cancer cells with a multivalent PSMA inhibitor-guided streptavidin conjugate, Bioorg. Med. Chem. Lett. 22 (12) (2012) 3931–3934, https://doi.org/10.1016/j.bmcl.2012.04.110.

[16] T. Wüstemann, et al., Targeting prostate cancer: prostate-specific membrane antigen-based diagnosis and therapy, Med. Res. Rev. 39 (1) (2019) 40–69, https://doi.org/10.1002/med.21508.

[17] T. Wüstemann, et al., Design of Internalizing PSMA-specific Glu-ureido-based Radiotherapeuticals, Theranostics 6 (8) (2016) 1085–1095, https://doi.org/10.7150/thno.13448.

[18] G. Ferro-Flores, et al., Clinical translation of a PSMA inhibitor for ^{99m}Tc-based SPECT, Nucl. Med. Biol. 48 (2017) 36–44, https://doi.org/10.1016/j.nucmedbio.2017.01.012.

[19] T. Liu, D.E. Mendes, C.E. Berkman, Functional prostate-specific membrane antigen is enriched in exosomes from prostate cancer cells, Int. J. Oncol. 44 (3) (2014) 918–922, https://doi.org/10.3892/ijo.2014.2256.

[20] T. Hernández-Jiménez, et al., ^{177}Lu-DOTA-HYNIC-Lys(Nal)-Urea-Glu: synthesis and assessment of the ability to target the prostate-specific membrane antigen, J. Radioanal. Nucl. Chem. 318 (3) (2018) 2059–2066, https://doi.org/10.1007/s10967-018-6239-9.

[21] F. Locardi, et al., Facile synthesis of NIR and visible luminescent Sm^{3+} doped lutetium oxide nanoparticles, Mater. Res. Bull. 86 (2017) 220–227, https://doi.org/10.1016/j.materresbull.2016.11.011.

[22] J. Johny, et al., Facile and fast synthesis of SnS_2 nanoparticles by pulsed laser ablation in liquid, Appl. Surf. Sci. 435 (2018) 1285–1295, https://doi.org/10.1016/j.apsusc.2017.11.243.

[23] P. Kim, et al., Trends in structure and thermodynamic properties of normal rare earth carbonates and rare earth hydroxycarbonates, Minerals 8 (3) (2018) 106–130, https://doi.org/10.3390/min8030106.

[24] N.A. Dulina, et al., Synthesis and characterization of the crystalline powders on the basis of Lu_2O_3: Eu^{3+} spherical submicron-sized particles, J. Eur. Ceram. Soc. 30 (7) (2010) 1717–1724, https://doi.org/10.1016/j.jeurceramsoc.2010.01.019.

[25] J.C. Soares, et al., Synthesis of $SmLuO_3$ and $EuLuO_3$ interlanthanides from hydrothermally-derived nanostructured precursors, Arab. J. Chem. 12 (8) (2019) 4035–4043, https://doi.org/10.1016/j.arabjc.2016.03.010.

[26] Q. Chen, et al., Fabrication and photoluminescence characteristics of Eu^{3+}-doped Lu_2O_3 transparent ceramics, J. Am. Ceram. Soc. 89 (6) (2006) 2038–2042, https://doi.org/10.1111/j.1551-2916.2006.01016.x.

[27] M. Runowski, N. Stopikowska, S. Lis, UV-Vis-NIR absorption spectra of lanthanide oxides and fluorides, Dalton Trans. 49 (7) (2020) 2129–2137, https://doi.org/10.1039/c9dt04921e.

[28] M.J. Mendoza-Figueroa, et al., Preparation and preclinical evaluation of ^{68}Ga-iPSMA-BN as a potential heterodimeric radiotracer for PET-imaging of prostate cancer, J. Radioanal. Nucl. Chem. 318 (3) (2018) 2097–2105, https://doi.org/10.1007/s10967-018-6285-3.

[29] D. Amans, et al., Synthesis of oxide nanoparticles by pulsed laser ablation in liquids containing a complexing molecule: impact on size distributions and prepared phases, J. Phys. Chem. C 115 (12) (2011) 5131–5139, https://doi.org/10.1021/jp109387e.

[30] D. Manzanares, V. Cena, Endocytosis: the nanoparticle and submicron nanocompounds gateway into the cell, Pharmaceutics 12 (4) (2020) 371–391, https://doi.org/10.3390/pharmaceutics12040371.

[31] K. Kettler, et al., Cellular uptake of nanoparticles as determined by particle properties, experimental conditions, and cell type, Environ. Toxicol. Chem. 33 (2014) 481–492, https://doi.org/10.1002/etc.2470.

[32] E. Gourni, et al., (R)-NODAGA-PSMA: a versatile precursor for radiometal labeling and nuclear imaging of PSMA-positive tumors, PLoS One 10 (12) (2015) e0145755, https://doi.org/10.1371/journal.pone.0145755.

[33] G. Ferro-Flores, et al., Multifunctional radiolabeled nanoparticles for targeted therapy, Curr. Med. Chem. 21 (1) (2014) 124–138, https://doi.org/10.2174/09298673113209990218.

[34] Y. Tolkach, et al., Prostate-specific membrane antigen expression in hepatocellular carcinoma: potential use for prognosis and diagnostic imaging, Oncotarget 10 (41) (2019) 4149–4160, https://doi.org/10.18632/oncotarget.27024.
[35] A. Sasikumar, et al., ^{68}Ga-PSMA PET/CT imaging in primary hepatocellular carcinoma, Eur. J. Nucl. Med. Mol. Imaging 43 (4) (2016) 795–796, https://doi.org/10.1007/s00259-015-3297-x.
[36] P. Backhaus, et al., Targeting PSMA by radioligands in non-prostate disease-current status and future perspectives, Eur. J. Nucl. Med. Mol. Imaging 45 (5) (2018) 860–877, https://doi.org/10.1007/s00259-017-3922-y.
[37] M.S. Bhangoo, et al., Radioembolization with Yttrium-90 microspheres for patients with unresectable hepatocellular carcinoma, J Gastrointest Oncol 6 (5) (2015) 469–478, https://doi.org/10.3978/j.issn.2078-6891.2015.056.
[38] A. Saini, et al., History and evolution of yttrium-90 radioembolization for hepatocellular carcinoma, J. Clin. Med. (2019) 8(1), https://doi.org/10.3390/jcm8010055.
[39] K.Y. Zhang, et al., Long-lived emissive probes for time-resolved photoluminescence bioimaging and biosensing, Chem. Rev. 118 (4) (2018) 1770–1839, https://doi.org/10.1021/acs.chemrev.7b00425.
[40] M.C. Heffern, L.M. Matosziuk, T.J. Meade, Lanthanide probes for bioresponsive imaging, Chem. Rev. 114 (8) (2014) 4496–4539, https://doi.org/10.1021/cr400477t.
[41] K. Binnemans, Lanthanide-based luminescent hybrid materials, Chem. Rev. 40 (50) (2009) 4283–4374, https://doi.org/10.1002/chin.200950225.
[42] J.S. Klein, C. Sun, G. Pratx, Radioluminescence in biomedicine: physics, applications, and models, Phys Med Biol 64 (4) (2019) 04TR01, https://doi.org/10.1088/1361-6560/aaf4de.
[43] Z. Farka, et al., Nanoparticle-based immunochemical biosensors and assays: recent advances and challenges, Chem. Rev. 117 (15) (2017) 9973–10042, https://doi.org/10.1021/acs.chemrev.7b00037.
[44] A. Bagheri, et al., Lanthanide-doped upconversion nanoparticles: emerging intelligent light-activated drug delivery systems, Adv Sci 3 (7) (2016) 1500437, https://doi.org/10.1002/advs.201500437.